

Chapter 1

Nuclear Magnetic Resonance as a Probe of Strongly Correlated Electron Systems

Nicholas J. Curro

Abstract Beginning with the pioneering NMR experiments of Hebel and Slichter in superconducting Aluminum, nuclear magnetic resonance (NMR) has played a central role in the study of strongly correlated electron matter. The relatively small energies associated with the nuclear spin degrees of freedom guarantee that the experimental probes of the nuclear spin behavior have little or no effect on the electronic degrees of freedom. On the other hand, the hyperfine coupling between the electronic and nuclear spins enables one to probe the static and dynamic properties of the electron spins through their effect on the nuclei. NMR offers detailed microscopic information about homogeneity, dynamics, and novel phases of electron matter and can probe under extreme conditions of high magnetic field, ultra low temperature, and high pressures. This chapter discusses the basics of NMR in condensed matter solids, including basic measurements such as the Knight shift, the hyperfine field, and the relaxation rates. To illustrate these concepts we discuss the case of field-induced antiferromagnetism and the exotic superconducting phase in CeCoIn₅.

1.1 Basics of Nuclear Magnetic Resonance

1.1.1 NMR Spectra

The energy of a nuclear magnetic moment in a magnetic field is given by the Zeeman Hamiltonian:

$$\begin{aligned}\mathcal{H}_Z &= \boldsymbol{\mu} \cdot \mathbf{H}_0 \\ &= \gamma \hbar \hat{\mathbf{I}} \cdot \mathbf{H}_0 \\ &= \hbar \omega_L \hat{I}_z,\end{aligned}\tag{1.1}$$

N.J. Curro (✉)

Department of Physics, University of California, Davis, CA 95616, USA
e-mail: curro@physics.ucdavis.edu

© Springer-Verlag Berlin Heidelberg 2015

A. Avella and F. Mancini (eds.), *Strongly Correlated Systems*,

Springer Series in Solid-State Sciences 180, DOI 10.1007/978-3-662-44133-6_1

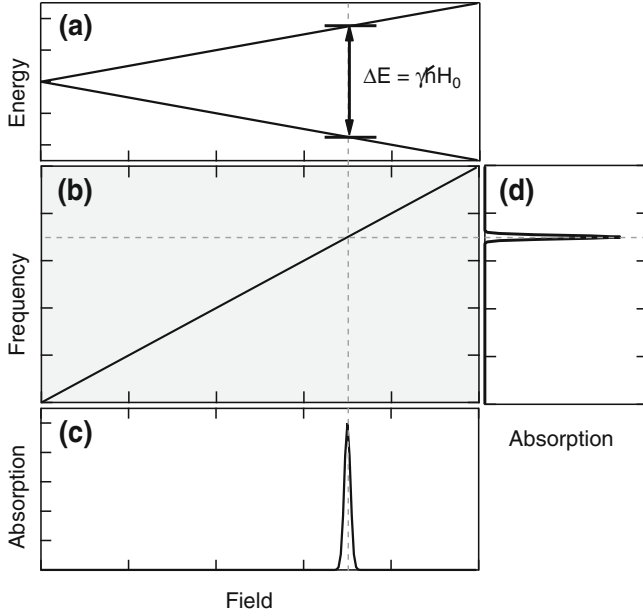


Fig. 1.1 **a** Energy levels for a spin $\frac{1}{2}$ in a magnetic field, **b** resonance frequency versus field, **c** field-swept spectrum at constant frequency, and **d** frequency-swept spectrum at constant field

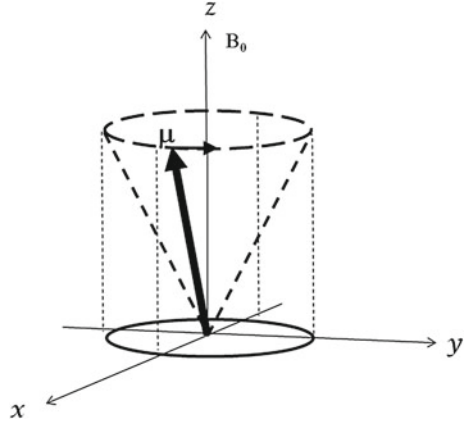
where γ is the gyromagnetic ratio, \hbar is Planck's constant, $\hat{\mathbf{I}} = \hat{I}_x \hat{x} + \hat{I}_y \hat{y} + \hat{I}_z \hat{z}$ is the nuclear spin operator, $\mathbf{H}_0 = H_0 \hat{z}$ is the magnetic field and $\omega_L = \gamma H_0$ is the Larmor frequency. For a spin $I = \frac{1}{2}$ nucleus we have:

$$\mathcal{H}_Z = \begin{pmatrix} \frac{\hbar\omega_L}{2} & 0 \\ 0 & -\frac{\hbar\omega_L}{2} \end{pmatrix} \quad (1.2)$$

The solution of this equation is straightforward: the eigenstates are $|\phi_m\rangle = |m\rangle$ with energy $E_m = \hbar\omega_L m$, where $m = \pm\frac{1}{2}$ and the splitting is $\Delta E = \hbar\omega_L$. The energy levels are shown in Fig. 1.1 as a function of magnetic field. There is a single resonance at the Larmor frequency. For higher spin nuclei there are $2I$ separate resonances, and depending on other terms in the Hamiltonian there can be considerable more structure in the spectra.

Nuclei transition between levels by absorbing or emitting a photon of energy $\hbar\omega_L$. In a typical NMR experiment, an ensemble of $\sim 10^{23}$ nuclei is located in a tuned radiofrequency coil that generates an electromagnetic field oscillating at the Larmor frequency, and power will be transferred between the nuclear spin system and the electromagnetic field. The spectrum is a measure of the absorbed power as a function of either the field, H_0 , or the frequency, ω , of the resonant circuit. Both approaches

Fig. 1.2 Precession of a magnetic moment, \mathbf{M} around a magnetic field, \mathbf{H}_0 oriented along the z -axis. The precession frequency is given by $\omega_L = \gamma H_0$, where γ is the gyromagnetic ratio



are complementary, and correspond to cuts across the frequency-field diagram in Fig. 1.1 along the vertical and horizontal axes, respectively. The absorption of power can be measured by detecting the response of a resonant circuit, such as a change in the quality factor of the resonance. Alternatively, the nuclei can be perturbed by resonant pulses of radiofrequency fields, and their response observed as a function of either field or frequency. This latter approach forms the basis of modern pulsed NMR and requires a detailed understanding of the time dependent response of the quantum mechanical system.

1.1.2 Density Matrix Solution

The wavefunction of the Hamiltonian in (1.2) is given by:

$$|\psi\rangle = ae^{i\omega_L t/2}|\uparrow\rangle + be^{-i(\omega_L t/2+\phi)}|\downarrow\rangle, \quad (1.3)$$

where the real constants a , b , and the phase factor ϕ depend on the initial conditions. Alternatively the solution can be expressed in terms of the density matrix:

$$\rho = \begin{pmatrix} a^2 & abe^{i(\omega_L t+\phi)} \\ abe^{-i(\omega_L t+\phi)} & b^2 \end{pmatrix}. \quad (1.4)$$

The diagonal elements are time independent and the off-diagonal elements oscillate at the Larmor frequency. The expectation values of the nuclear magnetization $\langle M_\alpha \rangle = \gamma \hbar \text{Tr}[\rho(t)\hat{I}_\alpha]$ are given by:

$$\langle I_x \rangle = ab \cos(\omega_L t + \phi) \quad (1.5)$$

$$\langle I_y \rangle = ab \sin(\omega_L t + \phi) \quad (1.6)$$

$$\langle I_z \rangle = \frac{1}{2}(a^2 - b^2). \quad (1.7)$$

These equations describe the magnetization vector $\langle \mathbf{M} \rangle$ precessing around the magnetic field \mathbf{H}_0 at frequency ω_L (Fig. 1.2). Of course, if we start the system off in an eigenstate of \mathcal{H}_Z , then either a or b is zero, $\langle I_x \rangle = \langle I_y \rangle = 0$, and there is no time dependence of the expectation value. In order for the spins to precess, they must be in a superposition of the eigenstates of \mathcal{H}_Z .

1.1.2.1 Statistical Ensemble

The density matrix (1.4) is valid for a single spin- $\frac{1}{2}$ in a magnetic field. In real solids, there are $N \sim 10^{23}$ nuclei, each with its own phase, ϕ_j . The Hilbert space has dimensions of $(2I + 1)^N \times (2I + 1)^N$, which is intractable for anything more than a few spins. However, it turns out that for most cases of interest we can treat the spins as independent particles. Of course, the nuclei do interact with both the surrounding electrons and with one another, but these interactions are small compared with the Zeeman interaction and can be introduced perturbatively. In practice this is a very good assumption, since the nuclei in a solid sit far apart from one another (the typical spacing between nuclei in a solid is $\sim 10^{-10}$ m, whereas the nuclei have radii $\sim 10^{-15}$ m). On the other hand, it is exactly these interactions both with one another and their environment that renders magnetic resonance such a powerful technique to probe the behavior of solids.

For N independent spins the density matrix has the form:

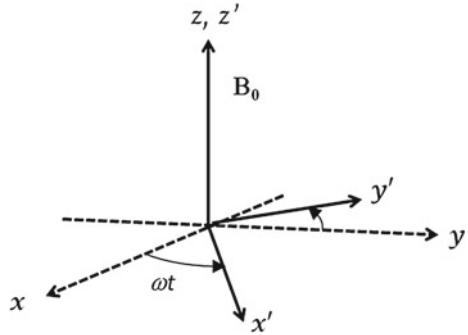
$$\hat{\rho}_N = \begin{pmatrix} a_1^2 & a_1 b_1 f(t) e^{i\phi_1} & \dots & 0 & \dots & 0 \\ a_1 b_1 f(t) e^{i\phi_1} & b_1^2 & \dots & 0 & \dots & 0 \\ \vdots & \vdots & \ddots & \vdots & \dots & \vdots \\ 0 & 0 & \dots & a_N^2 & \dots & a_N b_N f(t) e^{i\phi_N} \\ 0 & 0 & \dots & a_N b_N f(t) e^{i\phi_N} & \dots & b_N^2 \end{pmatrix}, \quad (1.8)$$

where $f(t) = e^{i\omega_L t}$. The statistical ensemble density matrix is obtained by a partial trace over the N degrees of freedom:

$$\langle \hat{\rho} \rangle = \begin{pmatrix} \langle a^2 \rangle & \langle ab \rangle e^{i\omega_L t} \sum_N e^{-i\phi_j/N} \\ \langle ab \rangle e^{-i\omega_L t} \sum_N e^{i\phi_j/N} & \langle b^2 \rangle \end{pmatrix}, \quad (1.9)$$

where $\langle a^2 \rangle = \frac{1}{N} \sum_n a_n^2$, $\langle b^2 \rangle = \frac{1}{N} \sum_n b_n^2$, and $\langle ab \rangle = \frac{1}{N} \sum_n a_n b_n$. In equilibrium each spin will have a different phase and these phases will be uncorrelated, thus the average of the phase factors $e^{i\phi_j}$ vanishes:

Fig. 1.3 The rotating frame rotates around the z -axis at angular frequency ω



$$\lim_{N \rightarrow \infty} \frac{1}{N} \sum_{j=1}^N e^{i\phi_j} = 0. \quad (1.10)$$

The off-diagonal matrix elements of the ensemble average density matrix, $\langle \rho \rangle$, are zero in thermal equilibrium. If the system is disturbed from thermal equilibrium (for example by pulsed NMR techniques), then these off-diagonal elements become finite and time dependent. The diagonal elements $\langle a^2 \rangle$ and $\langle b^2 \rangle$ for the ensemble average are simply the statistical probabilities of finding the spin in either the up or down state: $\langle a^2 \rangle, \langle b^2 \rangle = \frac{1}{Z} e^{\pm \beta \hbar \omega_L / 2}$, where $\beta = 1/k_B T$, k_B is the Boltzmann constant, T is the temperature, and $Z = e^{-\hbar \omega_L / 2 k_B T} + e^{\hbar \omega_L / 2 k_B T}$ is the partition function. Since $\pm \frac{1}{2} \hbar \omega_L$ are the eigenvalues of \mathcal{H}_Z , we can write the thermal equilibrium ensemble average density matrix as:

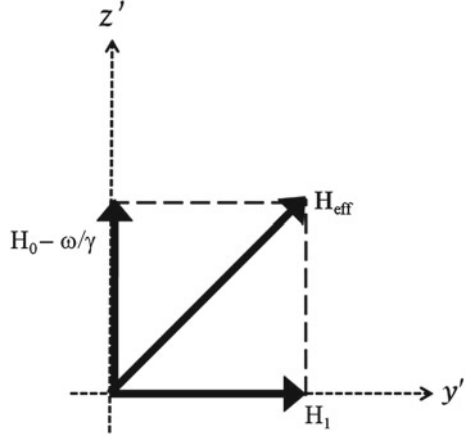
$$\rho_{EQ} = \frac{1}{Z} e^{-\beta \mathcal{H}_Z}, \quad (1.11)$$

where $\beta = 1/k_B T$. One can then calculate various thermodynamic quantities of interest associated with the nuclei using this formalism, such as the nuclear magnetization, M , the specific heat, C_n , and the magnetic susceptibility, χ_n . It is important to note that there are two types of density matrices: ρ , the density matrix for a single particle, and $\langle \rho \rangle$, the statistical ensemble density matrix for a system of N spins. In most cases we will consider the statistical ensemble average density matrix, drop the bracket notation and simply refer to it as the “density matrix”. Care should be taken, however, to not confuse the case for a single spin.

1.1.2.2 The Rotating Frame

Modern NMR spectrometers detect the coherent precession of an ensemble of nuclear spins, which give rise to a time dependent magnetization that couples to the NMR circuit. In this case, the ensemble average density matrix is not in equilibrium, and off-diagonal elements are created by radiofrequency pulses. During such a

Fig. 1.4 In the rotating frame, the moments precess around the effective field, \mathbf{H}_{eff} , which lies perpendicular to \mathbf{H}_0 when the irradiation frequency, ω is equal to the Larmor frequency, $\omega_L = \gamma H_0$



pulse, the Hamiltonian becomes: $\mathcal{H} = \gamma\hbar[\hat{I}_z B_0 + \hat{I}_y H_1 \cos(\omega t)]$, where \mathbf{H}_1 is the radiofrequency field generated by the solenoid oscillating at ω along the coil direction (taken here to lie along \hat{y}) perpendicular to the external field \mathbf{H}_0 . Typically $H_1 \sim 10 - 100 \text{ Oe}$, whereas $H_0 \sim 10 - 100 \text{ kOe}$. In order to solve for the time dependence of the magnetization, it is useful to transform to the rotating frame, which is equivalent to the interaction picture (see Fig. 1.3). In the rotating frame, the state vector, Hamiltonian, and density matrix transform as:

$$|\psi\rangle_R = \hat{U}|\psi\rangle \quad (1.12)$$

$$\mathcal{H}_R = \hat{U}\mathcal{H}\hat{U}^\dagger - i\hbar\frac{\partial\hat{U}}{\partial t}\hat{U}^\dagger \quad (1.13)$$

$$\rho_R = \hat{U}\rho\hat{U}^\dagger, \quad (1.14)$$

where $\hat{U} = e^{i\omega t \hat{I}_z}$, and the subscript R corresponds to the rotating frame. The Hamiltonian can be written as $\mathcal{H}_R = \gamma\hbar \mathbf{H} \hat{\mathbf{I}} \cdot \mathbf{H}_{\text{eff}}$, where $\mathbf{H}_{\text{eff}} = (H_0 - \omega/\gamma)\hat{z} + H_1\hat{y}$ is the effective field in the rotating frame (Fig. 1.4). When the rf frequency ω is equal to the natural resonance frequency of the nuclei in the magnetic field, ω_L , then \mathbf{H}_{eff} has no component along the \hat{z} direction—only along \hat{y} . In other words, at resonance in the rotating frame the spins precess around \mathbf{H}_1 , not \mathbf{H}_0 . By selectively turning pulses on and off along different directions, one can therefore manipulate the spins to point in any direction and create off-diagonal resonances in the density matrix.

The time dependence of $\rho_R(t)$ is given by:

$$i\hbar\frac{\partial\rho_R}{\partial t} = [\mathcal{H}_R, \rho_R], \quad (1.15)$$

and since \mathcal{H}_R is time independent this equation can be solved to give:

$$\rho_R(t) = e^{i\mathcal{H}_R t/\hbar} \rho_R(0) e^{-i\mathcal{H}_R t/\hbar}. \quad (1.16)$$

This expression enables one to calculate the density matrix, and hence the expectation values of the magnetization, following a series of pulses of varying power and duration by realizing that the pulses act as unitary transformations on the density matrix.

Consider, for example, a radiofrequency pulse exactly on resonance ($\omega = \omega_L$) with intensity $H_1 = \Omega_1/\gamma$ for a time $t_p \ll 1/\omega_L$. In this case $\hat{U} = e^{i\Omega_1 t \hat{I}_y}$. Immediately following the pulse the density matrix is given by:

$$\rho(t_p) = e^{i\Omega_1 t_p \hat{I}_y} \rho_R(0) e^{-i\Omega_1 t_p \hat{I}_y}. \quad (1.17)$$

If we assume that we start off in thermal equilibrium, then $\rho_R(0) = \rho(0) = \rho_{\text{EQ}}$. Furthermore, for temperatures $T > \hbar\omega_L/k_B \sim 10^{-6}$ K it is reasonable to use the high temperature approximation:

$$\rho_{\text{EQ}} = \frac{1}{Z} e^{\beta \hat{\mathcal{H}}_Z} \approx \frac{1}{N} \left(\hat{1} + \beta \hbar \omega_L \hat{I}_z + \dots \right). \quad (1.18)$$

We shall be interested in calculating observables such as $\langle M_z \rangle = \gamma \hbar \text{Tr}\{\hat{\rho} \hat{I}_z\}$, in which case the first term of this expansion will vanish, and we can safely ignore it. Therefore, in the rotating frame the equilibrium density matrix is identical to that in the laboratory frame:

$$\rho_R(0) = \varepsilon e^{i\omega t \hat{I}_z} \hat{I}_z e^{-i\omega t \hat{I}_z} = \varepsilon \hat{I}_z, \quad (1.19)$$

where $\varepsilon = \beta \hbar \omega_L / N \ll 1$.

In order to determine the effect of the radiofrequency pulse, it is important to consider the effect of the unitary rotation transform $\hat{U}_y = e^{i\theta \hat{I}_y}$ on the operator \hat{I}_z . It can be shown that [1]:

$$e^{i\theta \hat{I}_y} \hat{I}_z e^{-i\theta \hat{I}_y} = \hat{I}_z \cos(\theta) - \hat{I}_x \sin(\theta). \quad (1.20)$$

Therefore the density matrix immediately following the pulse is given by:

$$\rho_R(t_p) = \varepsilon \left(\hat{I}_z \cos(\Omega_1 t_p) - \hat{I}_x \sin(\Omega_1 t_p) \right) \quad (1.21)$$

$$= \frac{\varepsilon}{2} \begin{pmatrix} -\cos(\Omega_1 t_p) & \sin(\Omega_1 t_p) \\ \sin(\Omega_1 t_p) & \cos(\Omega_1 t_p) \end{pmatrix}, \quad (1.22)$$

and for times following the pulse in the laboratory frame the density matrix is:

$$\rho(t) = \frac{\varepsilon}{2} \begin{pmatrix} -\cos(\Omega_1 t_p) & \sin(\Omega_1 t_p) e^{i\omega_L t/2} \\ \sin(\Omega_1 t_p) e^{-i\omega_L t/2} & \cos(\Omega_1 t_p) \end{pmatrix}. \quad (1.23)$$

By turning on the H_1 field for a time of length $t_p = \frac{\pi}{2\Omega_1}$ the diagonal elements can be completely converted to *off-diagonal* elements, which then give rise to a time dependent magnetization $\mathbf{M}(t)$ precessing perpendicular to \mathbf{H}_0 .

1.1.2.3 Bloch Equations

The effect of a pulse is identical both for an individual spin-1/2 nucleus and an ensemble of independent nuclei. In the latter case, the density matrix describes an ensemble average, and it is important to note that the pulse creates a *coherent* precession of the spins. In other words, all of the nuclei start off with the same phase following the pulse. For $\Omega_1 t_p = \pi/2$ (1.23) describes finite off-diagonal coherence indefinitely. This result cannot be correct, however, since $\rho(t)$ must decay to ρ_{EQ} , a *time-independent* result, for sufficiently long times. Eventually all of the precessing spins will lose their coherence and relax back to a time independent equilibrium Boltzmann distribution. These relaxation processes are due to interactions between the spins themselves and with their environment. The *Bloch equations* describe the time dependence of the spins with relaxation by including two phenomenological parameters:

$$\frac{dM_x}{dt} = \gamma(\mathbf{M} \times \mathbf{H})_x - \frac{M_x}{T_2} \quad (1.24)$$

$$\frac{dM_y}{dt} = \gamma(\mathbf{M} \times \mathbf{H})_y - \frac{M_y}{T_2} \quad (1.25)$$

$$\frac{dM_z}{dt} = \gamma(\mathbf{M} \times \mathbf{H})_z - \frac{M_0 - M_z}{T_1}. \quad (1.26)$$

Here $\mathbf{M} = \gamma\hbar\langle\mathbf{I}\rangle/V$ is the magnetization density, the constant $M_0 = \chi_n H_0$ is the equilibrium magnetization, and $\chi_n = N\gamma^2\hbar^2 I(I+1)/3k_B T$ is the nuclear spin susceptibility. The time constant T_2 is the transverse relaxation, or spin-spin decoherence time, and T_1 is the longitudinal relaxation, or spin-lattice relaxation time. The first terms in the Bloch equations describe precession, and the second set of terms describe relaxation of the spins to equilibrium. T_2 describes the relaxation of the off-diagonal terms in the ensemble average density matrix, and T_1 describes the relaxation of the diagonal terms. The spin-lattice relaxation time is the time scale for the ensemble of spins to acquire thermal equilibrium. The spin-decoherence time, which generally is *not* equivalent to T_1 , describes the decay of the off-diagonal terms in the density matrix. Alternatively, if we consider the expectation value $\langle\mathbf{M}\rangle = \gamma\hbar\text{Tr}\{\rho\hat{\mathbf{I}}\}$, then T_1 describes the relaxation of the z component of the magnetization and T_2 describes the relaxation of the x - and y -components. Following a pulse along the \hat{y} direction of duration $t_p = \pi/2\Omega_1$, the time dependence of the ensemble average density matrix is given by:

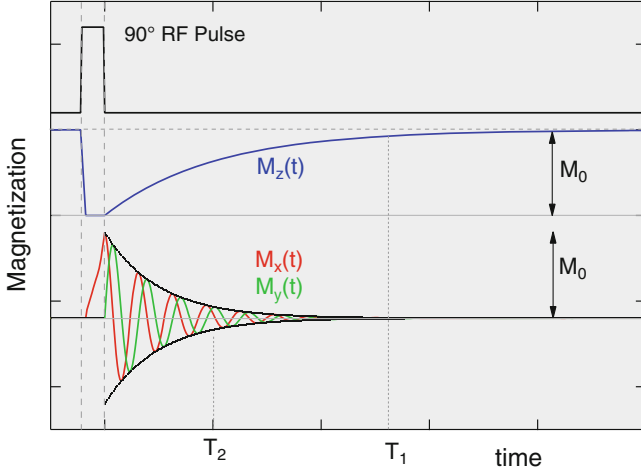


Fig. 1.5 Time dependence of the three components of the nuclear magnetization in the laboratory frame following a 90° radiofrequency pulse in the y -direction. In this case, $T_1 \gg T_2$, and $M_0 = \chi_n H_0$ is the equilibrium magnetization

$$\rho(t) = \frac{\varepsilon}{2} \begin{pmatrix} -(1 - e^{-t/T_1}) e^{i\omega_L t/2} e^{-t/T_2} \\ e^{-i\omega_L t/2} e^{-t/T_2} (1 - e^{-t/T_1}) \end{pmatrix}, \quad (1.27)$$

and the magnetization $\langle \mathbf{M} \rangle$ is:

$$\begin{aligned} M_x(t) &= \frac{1}{4} \gamma \hbar \varepsilon e^{-t/T_2} \cos(\omega_L t) \\ M_y(t) &= \frac{1}{4} \gamma \hbar \varepsilon e^{-t/T_2} \sin(\omega_L t) \\ M_z(t) &= \frac{1}{4} \gamma \hbar \varepsilon (1 - e^{-t/T_1}). \end{aligned} \quad (1.28)$$

These equations are plotted in Fig. 1.5. Note that T_2 describes the decay of the envelope of the transverse magnetization, and over a time scale T_1 the magnetization returns to equilibrium along the z -axis.

1.1.3 Pulse Techniques

The response of the magnetization following a pulse described by (1.28) is known as a Free Induction Decay or FID. The spectrum is given by the complex Fourier transform of the FID,

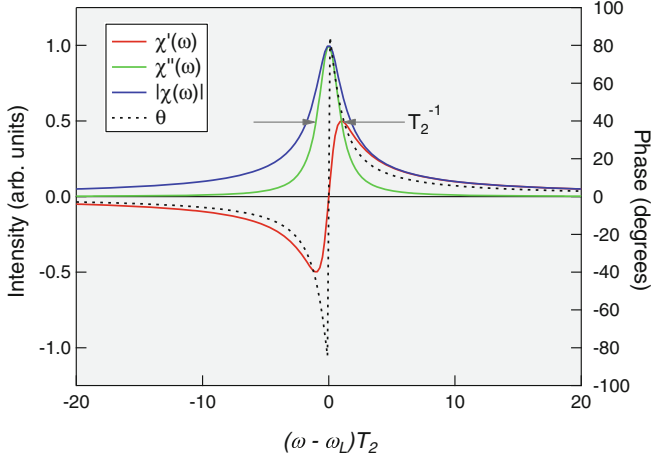


Fig. 1.6 Frequency dependence of the absorptive (red) and dispersive (green) components of the magnetization. Also shown are the magnitude (blue) and phase angle θ . The full width at half maximum of the resonance is given by T_2^{-1} . In a pulsed experiment, these correspond to the magnetization components along the two planar directions, where θ is defined relative to the phase of the original H_1 pulse

$$S(\omega) = \frac{1}{\sqrt{2\pi}} \int_{-\infty}^{\infty} M_+(t) e^{i\omega t} dt, \quad (1.29)$$

where $M_{\pm} = M_x \pm iM_y$. In this case it is given by:

$$S(\omega) = \frac{M_0}{2\pi} \frac{\omega_L T_2}{1 + i(\omega - \omega_L)T_2}. \quad (1.30)$$

The real and imaginary parts of $S(\omega)$ are the absorptive and dispersive parts of the spectrum, and are shown in Fig. 1.6. The spectrum is centered at ω_L and has a FWHM linewidth of $2T_2^{-1}$. $S(\omega)$ is measured usually by detecting the magnetization in real time and then taking the Fourier transform of the data. The components of the magnetization precessing perpendicular to \mathbf{H}_0 give rise to a voltage signal $V(t)$ across an NMR coil that is proportional to dM_y/dt . A typical phase sensitive spectrometer splits the detected signal $V(t)$ into two channels, then mixes it with internally generated signal $s_1(t) = s_0 \cos(\omega t)$ and $s_2(t) = s_0 \sin(\omega t)$. After mixing the signals in the two channels become:

$$s_1(t) \sim M_0 \omega_L [\sin((\omega - \omega_L)t) - \sin((\omega + \omega_L)t)] \quad (1.31)$$

$$s_2(t) \sim M_0 \omega_L [-\cos((\omega - \omega_L)t) + \cos((\omega + \omega_L)t)] \quad (1.32)$$

If $\omega \approx \omega_L$ then the first term will oscillate at very low frequency, and the second high frequency component can be eliminated by a low pass filter. Thus $s_1(t) \sim M_y(t)$ and $s_2(t) \sim M_x(t)$ are direct measures of the magnetization in the rotating frame. This is the basic operation of a *homodyne* quadrature receiver, and enables one to measure both the magnitude and phase of the magnetization.

There are several more complex types of receivers. For example a *heterodyne* receiver mixes $V(t)$ down to an intermediate frequency $\omega_I < \omega_L$. At this point, the signal could be passed through a narrow band-pass filter to reduce noise and then mixed down to DC in two channels which can then be digitized. However, modern data acquisition cards can digitize at rates up to several hundred MHz, which enables one to digitize either the intermediate signal at ω_I or even the original signal at ω_L . After digitization at these high frequencies, the signal can then be processed digitally to extract the magnitude and phase independently.

A serious problem with the detection of FIDs is that the voltage signal $V(t)$ in the NMR coil will ring for several time constants following a large rf pulse. Typical rf pulses induce voltages on the order of a hundred volts, whereas the precessing magnetization signal is often only μV in magnitude. Consequently there is a dead time of several ms during which the sensitive low-noise preamplifiers must be turned off in order to avoid saturation of the response. If T_2 is sufficiently short then it is possible that the FID will have decayed before the spectrometer can detect it. Quadrature detection is helpful in this regard because it enables one to vary the phase of the H_1 pulses in such a manner that the transient decay of the pulse ringing in the circuit can be canceled out, thus partially reducing the dead time.

1.1.3.1 Spin Echoes

In 1950, Erwin Hahn discovered a second magnetization signal in an NMR coil at a time $t = 2\tau$ if second 180° pulse is applied at a time τ after the first 90° pulse [2]. An NMR spin-echo arises because the ensemble of precessing spins that dephases during an FID can be refocused, and has the same time dependence as the FID itself. This enables one to detect the signal at a time τ after the end of the second pulse, during which time the voltage ringing can die down.

In order to understand the spin-echo, it is important to understand the origin of the decay of the FID signal. Equation (1.28) implies that the time dependence of the FID decay is determined by the time constant T_2 . T_2 was introduced as a phenomenological parameter, but what determines this quantity? The answer depends on details of the measuring equipment and the substance being measured. If the nuclei experience a distribution $P(H_{\text{loc}})$ of local magnetic fields, then there will be a distribution $P(\omega_L)$ of precession frequencies. If we assume a normal distribution $P(\omega_L) = \frac{1}{\sqrt{2\pi}\delta} \exp[(\omega_L - \omega_L^0)^2/2\delta^2]$, then in the time domain the signal is proportional to $e^{-\delta t} \cos(\omega_L^0 t)$. In other words, the measured decay time is $\delta^{-1} \equiv T_2^*$, which is equivalent to the *second moment of the local magnetic field distribution*. In the ensemble of $\sim 10^{23}$ spins, each one precesses at a slightly larger or slightly

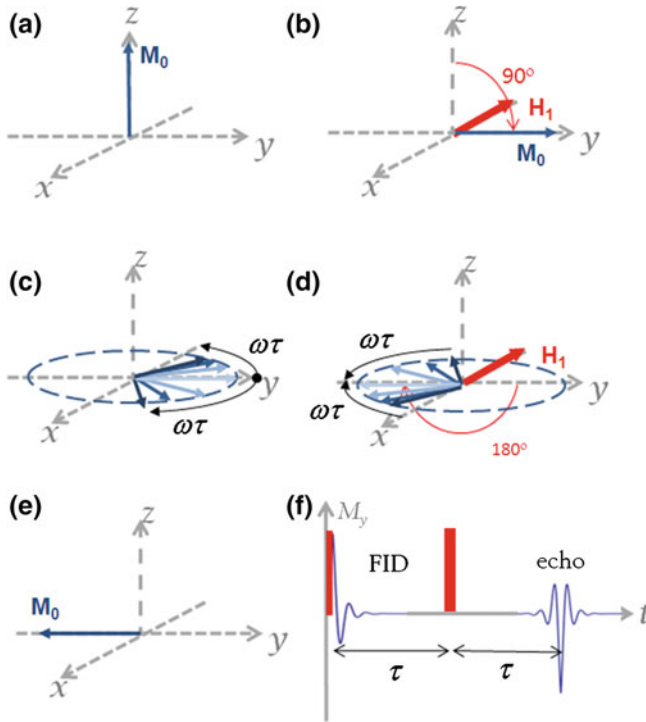


Fig. 1.7 A spin echo is formed by a two-pulse sequence. In this case, the sequence in panels (a)–(e) is $90^\circ_x - \tau - 180^\circ_x - \tau$ –echo. The FID forms along the $+y$ -direction in the rotating frame. Since M is the vector sum of all the individual spins, each with a slightly different precession frequency, the FID signal decays with time constant T_2^* as seen in panel (f). The second 180° pulse refocuses these spins a time 2τ after the first pulse. In this case, the echo forms along the $-y$ -direction

smaller rate than the average precession rate ω_L^0 so that in the rotating frame of ω_L^0 , the ensemble of spins will spread out around the plane over time. Eventually the net sum of these spins along the original axis will average to zero and the FID signal will decay with time constant T_2^* . T_2^* is often much smaller than the intrinsic T_2 of a material. This phenomenon is demonstrated in Fig. 1.7.

Two important sources of local magnetic field distributions are magnet inhomogeneity and dipole couplings between nuclei in a rigid lattice. Typically $\delta/\gamma \sim 0.01 - 10$ G for NMR magnets, and $\delta/\gamma \sim 100 - 1,000$ G for dipole couplings in solid materials. FIDs typically decay much faster in solids, in which case spin echoes are particularly important. Alternatively, the Fourier transform of the FID in a solid will be much broader than in a liquid. In both cases, however, the linewidth of the Fourier transform is given by $1/T_2^*$, which is not necessarily the intrinsic spin-decoherence time of the density matrix.

A classic analogy for the formation of a spin echo is a set of runners on a track. Initially all the runners are gathered in a pack at the starting line. When the gun

blows and the runners start racing, some will run faster and other will run slower. Eventually the pack of runners spreads out around the track. If the gun were shot a second time at which point each runner turns around and races backwards, then the pack of runners would return to the starting line exactly twice the time difference between the two gun shots. The fastest runners would have run the farthest and the slowest runners run the shortest distance, but the time to return to the starting line is the same for all the runners.

One apparent failure of this analogy is that the runners would tire after sufficient time, so that the longer time the run, the slower they become. If the second gun shot were to occur only 10s after the start of the race, then the entire pack would return simultaneously to the starting line 10s later. However if the second gun shot were to occur 10min after the start, it is doubtful that all the runners would return exactly 10min later in a well defined pack. The same effect occurs for the ensemble of nuclear spins, and is due to the loss of coherence in the density matrix. In other words, if $T_2^* \ll T_2$, then the FID signal (or the envelope of the echo) decays quickly, but echoes can still be formed as long as $\tau \lesssim T_2$. In fact, the intrinsic T_2 can be measured directly by measuring the echo size as a function of pulse spacing τ . In this case, the echo amplitude will decay as $e^{-2\tau/T_2}$.

1.1.3.2 Spin Lattice Relaxation

Any spin system that does not exhibit a Boltzmann population distribution among the energy levels is out of thermal equilibrium and will eventually return to equilibrium, in which all off-diagonal elements of the density matrix vanish and only the diagonal terms remain. This process is known as spin lattice relaxation, and can be measured with a sequence of three pulses:

$$180_x - t_1 - 90_x - \tau - 180_x - \tau - \text{echo}. \quad (1.33)$$

The first 180° pulse will invert the magnetization such that $M_z = -M_0$. The system then will return to equilibrium according to (1.24). The size of the magnetization at a time t_1 is measured by applying a two-pulse echo sequence to inspect $M_z(t_1)$. In this case, the magnetization is reversed by the first pulse, however other initial configurations are possible. For example, one could apply a 90° pulse, or a series of multiple 90° pulses known as a “comb” sequence. A comb sequence is intended to prepare the initial state such that $\langle M_x \rangle = \langle M_y \rangle = \langle M_z \rangle = 0$. Both types of preparatory pulses or pulse sequences simply change the initial conditions. For a spin 1/2 nucleus the recovery is single exponential, but for higher spin systems the recovery function is more complex, determined by a system of coupled differential equations.

1.2 Quadrupolar Nuclei

Approximately 71 % of all the isotopes with nuclear spins have $I > \frac{1}{2}$, and such nuclei manifest the full breadth and versatility of NMR as an experimental probe of the solid state. These isotopes are often referred to as quadrupolar nuclei since they experience an interaction between their electric quadrupolar moments and the local electrostatic potential in addition to any spin interactions. For $I > \frac{1}{2}$ there are multiple resonances corresponding to transitions between different nuclear spin levels. The spectra of such nuclei can be rich, complex, and challenging to interpret, but containing a wealth of information about the local electronic environment of the nuclei.

The quadrupolar interaction originates from the shape of a nucleus and its preferential orientation in the surrounding electrostatic environment usually created by the electrons. This interaction is given by:

$$\mathcal{H}_Q = \frac{1}{6} \sum_{\alpha\beta} \hat{Q}_{\alpha\beta} V_{\beta\alpha}, \quad (1.34)$$

where

$$Q_{\alpha\beta} = \int \rho_n(\mathbf{r})(3r_\alpha r_\beta - r^2 \delta_{\alpha\beta}) d^3r \quad (1.35)$$

are the elements of a quadrupolar tensor, where α and β are direction indices, and $\rho_n(\mathbf{r})$ is the nuclear charge density. The elements $V_{\beta\alpha} = \frac{\partial^2 V(0)}{\partial x_\alpha \partial x_\beta}$, where $V(\mathbf{r})$ is the electrostatic potential created by the electrons. $V_{\beta\alpha}$ form a second rank tensor in real space known as the Electric Field Gradient, or EFG tensor. The EFG is determined by the electronic system, and $Q_{\alpha\beta}$ is a property of the nucleus. Equation (1.34) describes the interaction between the nuclear quadrupolar moment and the EFG, but in this case the $Q_{\alpha\beta}$ are quantum mechanical operators that depend on the shape and orientation of the nucleus in the ground state manifold of I . By taking advantage of various quantum mechanical theorems and nuclear symmetries, this interaction can be written entirely in terms of spin operators and parameters of the EFG:

$$\mathcal{H}_Q = \frac{e^2 Q q}{4I(2I-1)} \left[(3\hat{I}_z^2 - \hat{I}^2) + \eta(\hat{I}_x^2 - \hat{I}_y^2) \right]. \quad (1.36)$$

Here Q is the quadrupolar moment of the nucleus, $eq \equiv V_{zz}$ is the largest eigenvalue of the EFG tensor, $\eta \equiv (V_{xx} - V_{yy}) / V_{zz}$ is the asymmetry parameter of the EFG. Q , like I , is an intrinsic parameter of the nucleus, and typically is on the order of a barn (10^{-24} cm^2). This expression is only valid in the basis which diagonalizes the EFG tensor, so that V_{xx} , V_{yy} and V_{zz} are the principal eigenvalues of the EFG tensor. For arbitrary directions the operators \hat{I}_α must be rotated using rotation operators. Usually the direction associated with the largest eigenvalue is notated \mathbf{q} and corresponds to $|V_{zz}| > |V_{xx}| > |V_{yy}|$.

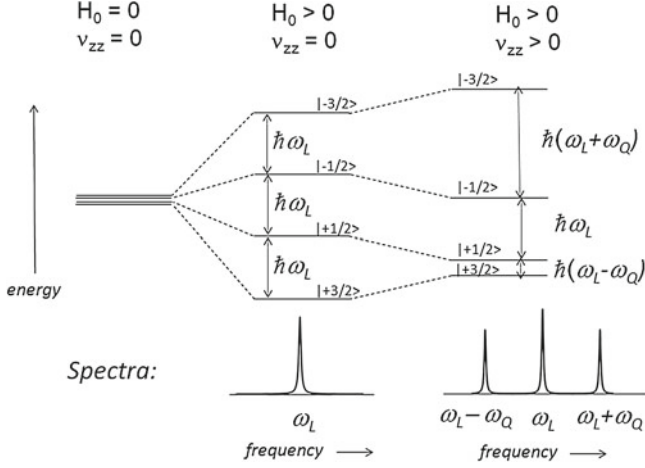


Fig. 1.8 A spin $I = 3/2$ nucleus in an external magnetic field \mathbf{H}_0 with an axial field gradient parallel to \mathbf{H}_0 has Hamiltonian $\mathcal{H} = \hbar\omega_L \hat{I}_z + \hbar\omega_Q(3\hat{I}_z^2 - \hat{I}^2)/6$. This system has three resonances split by the EFG

1.2.1 Quadrupolar Nuclei in Field

For a quadrupolar nucleus in a magnetic field the $2I + 1$ eigenstates are determined by $\mathcal{H}_Z + \mathcal{H}_Q$. In general \mathbf{H}_0 may not be in the same direction as one of the principal directions of the EFG tensor, in which case the Hamiltonian can quickly become difficult to diagonalize analytically. We will consider a simple case that captures the essential features of the spectrum of a quadrupolar nucleus and can still be solved analytically. Here \mathbf{H}_0 is parallel to \mathbf{q} and the EFG has axial symmetry ($\eta = 0$), so the total Hamiltonian is given by:

$$\mathcal{H} = \hbar\omega_L \hat{I}_z + \frac{\hbar\omega_Q}{6} (3\hat{I}_z^2 - \hat{I}^2), \quad (1.37)$$

where $\hbar\omega_Q \equiv \frac{3e^2qQ}{2I(2I-1)}$. Since \hat{I}_z commutes with \mathcal{H} , the Hamiltonian is diagonal in the \hat{I}_z basis. For $I = 3/2$ the eigenstates are given by:

$$|\phi_m\rangle = |m\rangle \quad (1.38)$$

$$\epsilon_m/\hbar = m\omega_L + \frac{4m^2 - 5}{8}\omega_Q = \begin{cases} -\frac{3}{2}\omega_L + \frac{1}{2}\omega_Q & \text{for } m = -\frac{3}{2} \\ -\frac{1}{2}\omega_L - \frac{1}{2}\omega_Q & \text{for } m = -\frac{1}{2} \\ +\frac{1}{2}\omega_L - \frac{1}{2}\omega_Q & \text{for } m = +\frac{1}{2} \\ +\frac{3}{2}\omega_L + \frac{1}{2}\omega_Q & \text{for } m = +\frac{3}{2}. \end{cases} \quad (1.39)$$

The transition frequencies (given by the selection rule $\Delta m = \pm 1$) are: $\omega_L - \omega_Q$, ω_L , and $\omega_L + \omega_Q$. The energy levels and the spectrum are shown in Fig. 1.8. Usually these three transitions are referred to the central ($-\frac{1}{2} \leftrightarrow \frac{1}{2}$) transition, and the satellites transitions ($\pm\frac{1}{2} \leftrightarrow \pm\frac{3}{2}$). The transition frequencies of each transition are linear in field:

$$\omega = \gamma H_0 \pm n\omega_Q, \quad (1.40)$$

where $n = -1, 0 + 1$. This behavior can be seen in the left panel of Fig. 1.9.

It is instructive to consider the behavior of the density matrix in this case. Previously we considered a spin-1/2 nucleus and found that the off diagonal terms of the density matrix oscillate at the Larmor frequency. For a higher spin nucleus, the off diagonal terms oscillate at a frequency $\omega_{\alpha\beta} = (\epsilon_\alpha - \epsilon_\beta)/\hbar$, where ϵ_α is the energy of the i th eigenstate and corresponds to the $i \leftrightarrow j$ transition. Each one of these off-diagonal elements corresponds to one of the possible nuclear spin transitions.

Consider such a system initially in equilibrium that experiences a 90° rotation about the y -axis. Following the rotation, the density matrix will evolve as:

$$\hat{\rho} = \begin{pmatrix} \frac{3}{2} & 0 & 0 & 0 \\ 0 & \frac{1}{2} & 0 & 0 \\ 0 & 0 & -\frac{1}{2} & 0 \\ 0 & 0 & 0 & -\frac{3}{2} \end{pmatrix} \xrightarrow{90_y^\circ} \begin{pmatrix} 0 & \frac{\sqrt{3}}{2} & 0 & 0 \\ \frac{\sqrt{3}}{2} & 0 & 1 & 0 \\ 0 & 1 & 0 & \frac{\sqrt{3}}{2} \\ 0 & 0 & \frac{\sqrt{3}}{2} & 0 \end{pmatrix} \xrightarrow{e^{i\gamma H t/\hbar}} \begin{pmatrix} 0 & \frac{\sqrt{3}}{2} e^{i(\omega_L + \omega_Q)t} & 0 & 0 \\ \frac{\sqrt{3}}{2} e^{-i(\omega_L + \omega_Q)t} & 0 & e^{i\omega_L t} & 0 \\ 0 & e^{-i\omega_L t} & 0 & \frac{\sqrt{3}}{2} e^{i(\omega_L - \omega_Q)t} \\ 0 & 0 & \frac{\sqrt{3}}{2} e^{-i(\omega_L - \omega_Q)t} & 0 \end{pmatrix}. \quad (1.41)$$

In this case, the off-diagonal elements oscillate at one of the three transition frequencies. The expectation value for the magnetization is:

$$\langle M_x \rangle = \frac{3}{2} \cos((\omega_L - \omega_Q)t) + 2 \cos(\omega_L t) + \frac{3}{2} \cos((\omega_L + \omega_Q)t). \quad (1.42)$$

(Note that the spectrum $S(\omega)$ is the Fourier transform of $\langle M_x \rangle$.) This equation indicates that there will be three resonances at $\omega_L - \omega_Q$, ω_L and $\omega_L + \omega_Q$, with relative intensities given by the ratio 3 : 4 : 3. The intensity of the transition between the $|m\rangle$ and $|m+1\rangle$ level is given by the square of the matrix element $(\hat{I}_+)^2_{m,m+1} = I(I+1) - m(m+1)$. For higher spin nuclei there will be more transitions, each with relative intensity given by this formula.

The 90° rotation needed to generate these off-diagonal elements must be generated by an H_1 pulse. If this pulse has components of frequency at each of the three transitions, then each off-diagonal matrix element will be generated as shown above. This is possible if the pulse length is short enough such that the frequency bandwidth of the pulse is wider than the difference between the resonances; in other words, if

$t_p < (2\omega_Q)^{-1}$. This condition may not be possible in general, since ω_Q can vary anywhere from a few kHz to several MHz whereas t_p is typically on the order of a microsecond or longer. The broadest coverage of a resonance is typically less than about 1 MHz, so if $\omega_Q > 500$ kHz, then not all of the transitions can be excited simultaneously. In some cases, one can use special frequency-swept excitation pulses, or special pulse sequences to excite all of the transitions [3]. Alternatively, one can excite and detect each resonance independently of one another.

Consider the effect of a 90° pulse at the lower satellite transition of the spin $\frac{3}{2}$ case discussed above. The Hamiltonian in the rotating frame is:

$$\mathcal{H}_R = \hbar(\omega_L - \omega)\hat{I}_z + \hbar\frac{\omega_Q}{6}(3\hat{I}_z^2 - I^2) + \hbar\Omega_1\hat{I}_y \quad (1.43)$$

$$= \hbar \begin{pmatrix} \frac{(3\omega_L + \omega_Q - 3\omega)}{2} & -\frac{1}{2}i\sqrt{3}\Omega_1 & 0 & 0 \\ \frac{1}{2}i\sqrt{3}\Omega_1 & \frac{(\omega_L - \omega_Q - \omega)}{2} & -i\Omega_1 & 0 \\ 0 & i\Omega_1 & \frac{(\omega - \omega_L - \omega_Q)}{2} & -\frac{1}{2}i\sqrt{3}\Omega_1 \\ 0 & 0 & \frac{1}{2}i\sqrt{3}\Omega_1 & \frac{(3\omega - 3\omega_L + \omega_Q)}{2} \end{pmatrix}.$$

In principle we can compute the solution to the density matrix by using the operator $\hat{T}(t) = e^{i\mathcal{H}_R t/\hbar}$ since \mathcal{H}_R is independent of time. However, this quickly becomes intractable even when ω matches one of the three resonance frequencies because there is no closed form expression for the operator $\hat{T}(t)$.

In order to make headway, note that we only really care about the first off diagonal elements of the density matrix, not the entire density matrix itself. Furthermore, we only are interested in one particular transition at a time. In this case, we can focus on the subspace of Hilbert space corresponding to the two eigenstates of the transition in question:

$$\begin{pmatrix} \frac{1}{2}(3\omega_L + \omega_Q - 3\omega) & -\frac{1}{2}i\sqrt{3}\Omega_1 & 0 & 0 \\ \frac{1}{2}i\sqrt{3}\Omega_1 & \frac{1}{2}(\omega_L - \omega_Q - \omega) & -i\Omega_1 & 0 \\ 0 & i\Omega_1 & \frac{1}{2}(\omega - \omega_L - \omega_Q) & -\frac{1}{2}i\sqrt{3}\Omega_1 \\ 0 & 0 & \frac{1}{2}i\sqrt{3}\Omega_1 & \frac{1}{2}(3\omega - 3\omega_L + \omega_Q) \end{pmatrix}.$$

We can consider the two upper levels as an effective spin- $\frac{1}{2}$ system, with Hamiltonian:

$$\mathcal{H}_{\text{eff}} = \hbar \begin{pmatrix} \frac{1}{2}(3\omega_L + \omega_Q - 3\omega) & -\frac{1}{2}i\sqrt{3}\Omega_1 \\ \frac{1}{2}i\sqrt{3}\Omega_1 & \frac{1}{2}(\omega_L - \omega_Q - \omega) \end{pmatrix}. \quad (1.44)$$

If $\omega = \omega_L + \omega_Q$, then

$$\mathcal{H}_{\text{eff}} = \hbar \begin{pmatrix} -\omega_Q & -\frac{1}{2}i\sqrt{3}\Omega_1 \\ \frac{1}{2}i\sqrt{3}\Omega_1 & -\omega_Q \end{pmatrix} = -\hbar\omega_Q\hat{\mathbb{I}} + \hbar\frac{\sqrt{3}}{2}\Omega_1\hat{I}_y. \quad (1.45)$$

The first term is just a constant offset, and the second term indicates that the effective field lies along the y axis, with amplitude $\frac{\sqrt{3}}{2}\Omega_1/\gamma$. This means that the magnetization of the effective spin- $\frac{1}{2}$ will precess around H_1 in the rotating frame, but at an enhanced precession rate. A 90° rotation would be enabled with a pulse width such that $\frac{\sqrt{3}}{2}\Omega_1 t_p = \frac{\pi}{2}$. The other transitions remain unaffected, so the density matrix evolves as:

$$\hat{\rho} = \begin{pmatrix} \frac{3}{2} & 0 & 0 & 0 \\ 0 & \frac{1}{2} & 0 & 0 \\ 0 & 0 & -\frac{1}{2} & 0 \\ 0 & 0 & 0 & -\frac{3}{2} \end{pmatrix} \xrightarrow{90_y^\circ(\omega_L+\omega_Q)} \begin{pmatrix} 0 & \frac{\sqrt{3}}{2} & 0 & 0 \\ \frac{\sqrt{3}}{2} & 0 & 1 & 0 \\ 0 & 0 & -\frac{1}{2} & 0 \\ 0 & 0 & 0 & -\frac{3}{2} \end{pmatrix} \xrightarrow{e^{i\mathcal{H}t/\hbar}} \begin{pmatrix} 0 & \frac{\sqrt{3}}{2}e^{i(\omega_L+\omega_Q)t} & 0 & 0 \\ \frac{\sqrt{3}}{2}e^{-i(\omega_L+\omega_Q)t} & 0 & 0 & 0 \\ 0 & 0 & -\frac{1}{2} & 0 \\ 0 & 0 & 0 & -\frac{3}{2} \end{pmatrix}. \quad (1.46)$$

This example demonstrates that each of the quadrupolar satellites can be observed independently from one another, and that each transition has a particular resonance amplitude and effective H_1 field that depends on the transition and the spin of the nucleus.

1.2.1.1 Nuclear Quadrupolar Resonance

The simple relationship between the field H_0 and the resonance frequency for a spin $1/2$ system becomes more complex for higher spin nuclei. Equation (1.40) expresses this relationship for the simple case discussed above, and is shown in Fig. 1.9. There are clearly three sets of transitions, and even at $H_0 = 0$ there is a finite frequency. This zero field resonance corresponds to Nuclear Quadrupolar Resonance (NQR). In this case the two sets of states $|\pm \frac{3}{2}\rangle$ and $|\pm \frac{1}{2}\rangle$ are both degenerate, with an splitting given by $\hbar\omega_Q$. NQR is essentially identical to NMR except with the absence of a magnetic field. ω_Q is determined by the parameters of the crystal, and often one cannot determine the EFG a priori. In practice ω_Q is determined by measuring the spectrum in field prior to doing an NQR experiment. A significant advantage of NQR is that the absence of an external field means that there are no alignment issues for the crystal. In fact, NQR is often performed on a powder sample. Nuclei in any crystallites in the powder oriented such $\mathbf{q} \perp \mathbf{H}_1$ will be excited. NQR is particularly useful for measuring the internal field of magnetically ordered materials. In this case, the development of long range magnetic order generally gives rise to a static internal magnetic field, which shifts or splits the NQR resonance, as seen in Fig. 1.9 and in (1.40).

1.2.1.2 Angular Dependence

In cases where the Hamiltonian cannot be diagonalized analytically, it can often be solved either by perturbation theory or via numerical methods. This is the case for arbitrary orientation of \mathbf{H}_0 with respect to the EFG, and for $\eta \neq 0$. The frequency versus field relationship is shown in Figs. 1.9 and 1.10. In these plots, the intensity of the line is proportional to the intensity

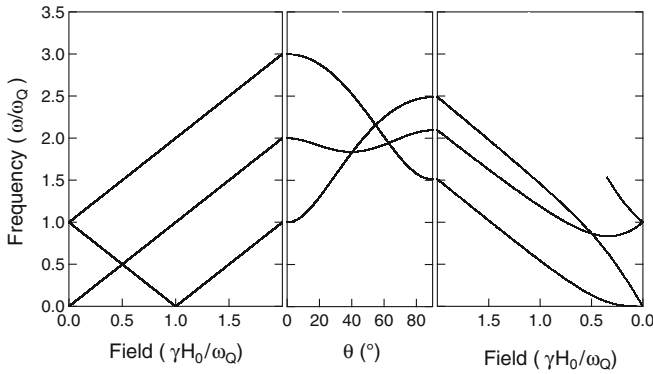


Fig. 1.9 The resonance frequencies of the Hamiltonian (1.37) for $I = 3/2$ and $\eta = 0$ as a function of field and angle. The normalized resonance frequency ω/ω_Q is plotted on the vertical axis, and the field is normalized as $\gamma H_0/\omega_Q$. The *left panel* shows the frequency versus field for $\theta = 0$ ($\mathbf{H}_0 \parallel \mathbf{q}$), the *center panel* shows the frequencies versus angle θ , and the *right panel* shows the frequencies versus field for $\theta = 90^\circ$

of the transition. The intensity of a transition between the states $|j\rangle$ and $|k\rangle$ is given by the square of the matrix element $|\langle j|\hat{I}_x|k\rangle|^2$. For most cases, this matrix element vanishes. If the eigenstates are given by the $|m\rangle$ states (such that \hat{I}_z is diagonal) then $\langle j|\hat{I}_x|k\rangle = 0$ unless $j = k \pm 1$ or $\Delta m = \pm 1$. This rule implies that there should be only $2I$ transition in the spectrum—for example Figs. 1.9 and 1.10 show three transitions for $I = \frac{3}{2}$. The only allowed transitions are those between adjacent levels because the field \mathbf{H}_1 couples to the \hat{I}_+ and \hat{I}_- operators, which can only raise or lower the state by one level. However, when $[\mathcal{H}, \hat{I}_z] \neq 0$ the eigenstates $|j\rangle$ are superpositions of the $|m\rangle$ states and it is possible that $\langle j|\hat{I}_x|k\rangle > 0$ for states that are not adjacent in energy and $\Delta m \neq \pm 1$ for such a transition. These are so-called “forbidden” transitions, and generally have weaker transition intensities because the matrix element $\langle j|\hat{I}_x|k\rangle$ is smaller. An example is seen in Fig. 1.9. For $\theta = 90^\circ$, $[\mathcal{H}_Q, \mathcal{H}_Z] \neq 0$, and for low fields ($H_0 \ll \omega_Q/\gamma$) there are more than just $2I$ transitions possible. In this case a fourth weaker transition is evident, as seen on the right hand side of the Figure. The same phenomenon is visible for $\eta \neq 0$ in Fig. 1.10. For sufficiently large fields H_0 , the matrix element $|\langle j|\hat{I}_x|k\rangle|^2$ becomes too small to detect the transition.

Plots of frequency versus field such as Figs. 1.9 and 1.10 are critical to understanding the spectra of single crystals with high spin nuclei. In practice it can be difficult to identify a particular resonance, which depends on both the orientation as well as the EFG parameters eq and η . Careful measurements at either constant frequency or constant field, as well as angle rotational studies, are key to identifying the various NMR quantities such as the EFG and the magnetic shift (discussed below).

1.3 Hyperfine Couplings

In the previous discussion of the Bloch equations, the parameters T_1 and T_2 were introduced as phenomenological parameters to take into account the effect of interactions among nuclear spins and their environment. These interactions can include magnetic dipolar interactions

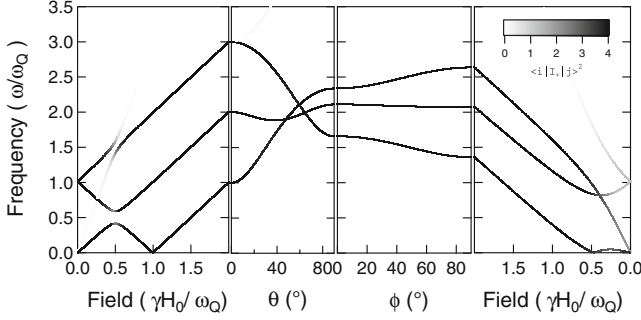


Fig. 1.10 The resonance frequencies of the Hamiltonian (1.34) for $I = 3/2$ and $\eta = 0.3$ as a function of field and angle. The normalized resonance frequency ω/ω_Q is plotted on the vertical axis, and the field is normalized as $\gamma H_0/\omega_Q$. The *left panel* shows the frequency versus field for $\theta = 0$ ($\mathbf{H}_0 \parallel \mathbf{q}$), the *two center panels* shows the frequencies versus the angles θ and ϕ , respectively, and the *right panel* shows the frequencies versus field for $\theta = \phi = 90^\circ$. The square of the matrix element of the transition is shown on the gray scale legend. For some range of parameters, the transitions “fade out”—these are “forbidden” transitions

among neighboring nuclei or with nearby electrons. In fact, one of the most important interaction for nuclei in condensed matter and strongly correlated systems is the hyperfine interaction, coupling the nuclear spins to the electron spins:

$$\begin{aligned}\mathcal{H}_{\text{hyp}} &= A \hat{\mathbf{I}} \cdot \mathbf{S} \\ &= A \hat{I}_z S_z + \frac{1}{2} A (\hat{I}_+ S_- + \hat{I}_- S_+),\end{aligned}\quad (1.47)$$

where A is the hyperfine constant, typically on the order of 10^{-8} eV. This constant is often expressed as $A/\gamma \hbar \mu_B$ in units of Oe/ μ_B . Typical values are on the order of $10 \text{ kOe}/\mu_B$. This unit is often more useful since it gives an estimate of the size of the hyperfine field that the electron spin creates at the nucleus. This coupling allows the nuclei to probe both the static susceptibility, χ_0 , and the dynamical susceptibility, $\chi(\mathbf{q}, \omega)$, of the electronic degrees of freedom. The diagonal term $A \hat{I}_z \hat{S}_z$ gives rise to a static shift of the resonance frequency.

1.3.1 Knight Shift

The Hamiltonian for a nucleus in an external field that experiences a hyperfine interaction is given by:

$$\mathcal{H} = \hbar \omega_L \hat{I}_z + A \hat{I}_z S_z. \quad (1.48)$$

For temperatures $T \gg A/k_B \sim 10^{-4}$ K, the electron and nuclear spins do not develop any coherence and therefore we can replace S_z with its thermal averaged value $\langle S_z \rangle = \chi H_0$, where χ is the magnetic susceptibility of the electronic system. The Hamiltonian can be rewritten then as:

$$\mathcal{H} = \hbar\omega_L(1 + K)\hat{I}_z, \quad (1.49)$$

where the Knight shift, K , measures the percent shift of the resonance frequency from that of an isolated nucleus ($\omega_0 = \gamma H_0$). The Knight shift is given by: $K = A\chi_0/\hbar\gamma\mu_B$. In a Fermi liquid, χ_0 is given by the Pauli susceptibility, so $K \sim AN(0)$ is temperature independent.

This scenario works well for simple metals such as Li and Na, yet there are many cases where the Knight shift is more complex. In Pt, for example, there are multiple hyperfine couplings to the d- and sp- bands, and hence several contributions to the total shift [4]. In many-electron atoms, there is also a core-polarization term, in which the core s electrons acquire a population difference between the up- and down-spin states. This difference arises because the orthogonal eigenstates of the many-electron atom get mixed by the perturbing influence of the external field. In practice, it is difficult to estimate the contribution of a core-polarization term versus a purely contact term [5]. As a result, hyperfine couplings are usually taken to be material dependent parameters.

In metals with local moments, such as rare-earth and d-electron systems, there is also a second hyperfine coupling to these moments that give rise to a strong temperature dependence of the total shift [6]. In heavy fermion systems the hyperfine coupling is given by:

$$\mathcal{H}_{\text{hyp}} = \gamma\hbar\hat{\mathbf{I}} \cdot (\mathbb{A} \cdot \mathbf{S}_c + \mathbb{B} \cdot \mathbf{S}_f), \quad (1.50)$$

where \mathbb{A} is an on-site hyperfine tensor interaction to the conduction electron spin, and \mathbb{B} is a transferred hyperfine tensor to the f spins [7]. Note that we consider here nuclear spins on the ligand sites, i.e., not on the f atom nucleus.

Given the two spin species, S_c and S_f , there are three different spin susceptibilities: $\chi_{cc} = \langle S_c S_c \rangle$, $\chi_{cf} = \langle S_c S_f \rangle$, and $\chi_{ff} = \langle S_f S_f \rangle$. The full expression for the Knight shift is given by:

$$K(T) = A\chi_{cc}(T) + (A + B)\chi_{cf}(T) + B\chi_{ff}(T). \quad (1.51)$$

where we have absorbed the g-factors into the definition of the hyperfine constants and dropped the tensor notation for notational simplicity [7]. The bulk susceptibility is given by:

$$\chi(T) = \chi_{cc}(T) + 2\chi_{cf}(T) + \chi_{ff}(T). \quad (1.52)$$

Note that if $A = B$, then $K \propto \chi$ for all temperatures. However, if $\chi_{cc}(T)$, $\chi_{cf}(T)$, and $\chi_{ff}(T)$ have different temperature dependences, then the Knight shift will not be proportional to susceptibility, leading to a Knight shift anomaly at a temperature T^* . This phenomenon is illustrated in Fig. 1.11. In this case both χ_{ff} and χ_{cf} have different temperature dependences, thus K and χ stop scaling with one another below $T^* \sim 60$ K. This temperature corresponds to the coherence temperature of the Kondo lattice in this compound [8, 9].

1.3.2 Spin Lattice Relaxation

The off diagonal terms of the hyperfine interaction couple neighboring transitions through the \hat{I}_{\pm} operators. This perturbation corresponds to a spin-flip exchange between the electron spin and the nuclear spin. These processes do not shift the resonance frequency, but do affect the dynamics of the nuclei. In fact, this process is crucial to bring about an equilibrium population

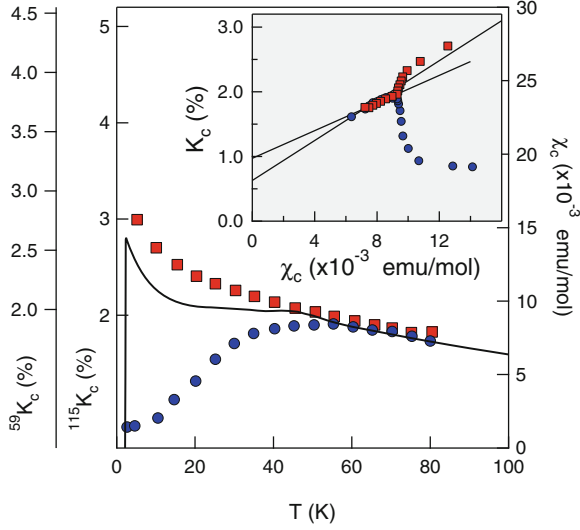


Fig. 1.11 The Knight shift of the In(1) (red squares) and the Co (blue circles) in CeCoIn₅, compared with the bulk susceptibility, $\chi(T)$ (solid line), in the c -direction. INSET: K_c [(In(1))] and K_c (Co) versus χ_c with temperature as an implicit parameter. The solid lines are linear fits to the data for $T > T^*$. T^* , the temperature where K and χ diverge, is approximately 50 K in this case

distribution among the nuclear spin levels. Consider a Fermi liquid with a simple contact interaction give by (1.50). As the quasiparticles scatter from one nucleus to another, they maintain essentially the same energy since the nuclear Zeeman energy is orders of magnitude lower than the Fermi level, and the quasiparticle Zeeman energy can be absorbed by states within $k_B T$ of E_F . By using Fermi's Golden Rule one can show that the spin-lattice-relaxation rate can be written as:

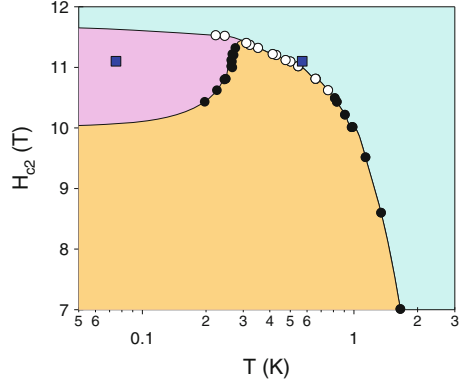
$$T_1^{-1} = \gamma^2 A^2 \int_0^\infty \langle \hat{S}_+(t) \hat{S}_-(0) \rangle e^{i\omega_0 t} dt, \quad (1.53)$$

where the brackets indicate a thermal averaged correlation function. In a Fermi liquid, the states available for scattering the quasiparticles are those at the Fermi surface, and by a simple counting argument one can show that (1.53) can be written as:

$$T_1^{-1} = \frac{\gamma^2 A^2}{2} \int_0^\infty N(E_i) N(E_f) f(E_i) (1 - f(E_f)) dE_i \quad (1.54)$$

where $E_f - E_i = \hbar\omega_0$. Since $f(E)(1 - f(E)) \approx k_B T \delta(E - E_F)$, we find that $T_1^{-1} \sim T A^2 N^2(0)$. In other words, measurements of T_1^{-1} yield information about the square of the density of quasiparticle states at the Fermi level. Any changes to the Fermi surface as a function of temperature, such as the development of a superconducting gap, will be reflected in T_1^{-1} . It is also immediately obvious that $T_1 T K^2 \equiv \mathcal{K}$ is constant in a Fermi liquid. This Korringa

Fig. 1.12 The phase diagram of CeCoIn₅ in high field as determined by specific heat [11]. *Solid points* represent second order phase transitions and *open points* are first order transitions. The *solid blue squares* are the points at which the spectra in Figs. 1.14 and 1.15 were obtained



constant, $\mathcal{K} = \pi^2 \hbar \gamma^2 / \mu_B^2$, is valid for non-interacting systems. In practice \mathcal{K} is found often to deviate from unity, which is usually taken as a measure of the strength of the quasiparticle interactions [10].

The expression (1.53) can be rewritten also in terms of the dynamical susceptibility:

$$T_1^{-1} = \gamma^2 k_B T \lim_{\omega \rightarrow 0} \sum_{\mathbf{q}} A^2(\mathbf{q}) \frac{\chi''(\mathbf{q}, \gamma)}{\hbar \omega}, \quad (1.55)$$

where the form factor $A^2(\mathbf{q})$ is the square of the Fourier transform of the hyperfine interaction, and the sum over \mathbf{q} is over the first Brillouin zone [12]. For a contact interaction, $A^2(\mathbf{q})$ is constant, but for more complex situations involving transferred couplings between neighboring sites, $A^2(\mathbf{q})$ can have structure and may vanish at particular wavevectors. A \mathbf{q} -dependent form factor can have profound consequences for the behavior of T_1^{-1} in materials. A notorious example is the difference in T_1^{-1} observed for the planar Cu and planar O in the cuprates [13]. Each nucleus has a different form factor and the dynamical susceptibility of this material is dominated by fluctuations at a particular wavevector, \mathbf{Q} . Since $A^2(\mathbf{q})$ vanishes for the O site but not for the Cu site, the two spin-lattice-relaxation rates have very different temperature dependences, even though they are coupled to the same degree of freedom, the Cu $3d^9 S = 1/2$ spins.

1.4 Case Study: Field Induced Magnetism

The heavy-fermion superconductor CeCoIn₅ has attracted considerable attention since its discovery in 2001, and NMR has played a central role in elucidating the novel physics of this strongly correlated electron system [14]. Of particular interest is a magnetic field induced phase (the Q phase) that emerges close to the upper critical field H_{c2} (see Fig. 1.12). This material is an unconventional d-wave superconductor that also exhibits non-Fermi liquid behavior associated with proximity to an antiferromagnetic quantum critical point. The normal state quasiparticles have an enhanced mass and a large magnetic susceptibility, and

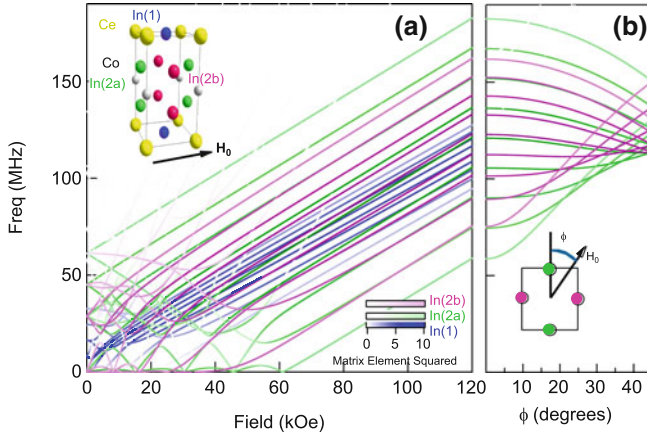


Fig. 1.13 **a** The frequency versus field relationship for the In(1) and In(2) sites in CeCoIn₅ for the field located in the ab plane. There are two distinct In(2) sites in this orientation because the field can point either parallel or perpendicular to the principal EFG axis, q . The *inset* shows the unit cell. **b** The position of the two In(2) resonances as a function of the angle, ϕ in the ab plane

consequently the superconducting state is Pauli limited [15]. This means that for sufficiently large magnetic fields the superconductivity is destroyed by breaking apart the Cooper pair singlets rather than by orbital currents as in more common orbital limited superconductors. In Pauli limited superconductors the condensate is expected theoretically to form long wavelength modulations in which the Cooper pairs develop finite momenta in certain limits [16–18]. This so-called Fulde-Ferrell-Larkin-Ovchinnikov (FFLO) superconducting phase was first predicted to exist in Pauli-limited superconductors several decades ago, but an experimental realization has proved elusive. The field-induced phase of CeCoIn₅ was identified initially as an FFLO phase based on bulk thermodynamic measurements [11, 19–21].

Subsequent NMR work, however, revealed a much more complex picture [22]. This material is ideal for NMR studies because there are multiple NMR active sites in the unit cell. There are two In sites per unit cell (^{115}In has spin $I = 9/2$), and one Co site (^{59}Co has spin $I = 7/2$). The In(1) site has axial symmetry and is located in the Ce-In plane, and the In(2) site has lower symmetry and is located on the lateral faces of the unit cell (see inset of Fig. 1.13). The EFG parameters of both sites are well known ($\nu_Q = 8.173\text{ MHz}$, $\eta = 0$ for the In(1) and $\nu_{zz} = 15.489\text{ MHz}$, $\eta = 0.386$ for the In(2), and the frequency versus field relationship for this material is shown in Fig. 1.13 [8]. In this case there are two In(2) sites since the external magnetic field can point either parallel or perpendicular to the unit cell face, and the principal axis of the EFG (q) points towards the center of the unit cell. These two sites are sometimes referred to In(2a) ($H_0 \parallel q$) and In(2b) ($H_0 \perp q \perp \hat{c}$). Thus there are four unique crystallographic sites that can be probed with NMR in the Q phase.

Initial NMR studies focused solely on the In(1) site and found dramatic changes to the Knight shift that were interpreted as evidence for the FFLO phase [21, 23, 24]. A more careful study looking at all four NMR sites revealed the presence of incommensurate antiferromagnetic order in contrast to the standard predictions for the FFLO phase [18, 22, 25]. Figures 1.14 and 1.15 show the In and Co spectra at constant field as a function of temperature. Each site clearly exhibits a different response in the Q phase. There is a discontinuity in the Knight shift

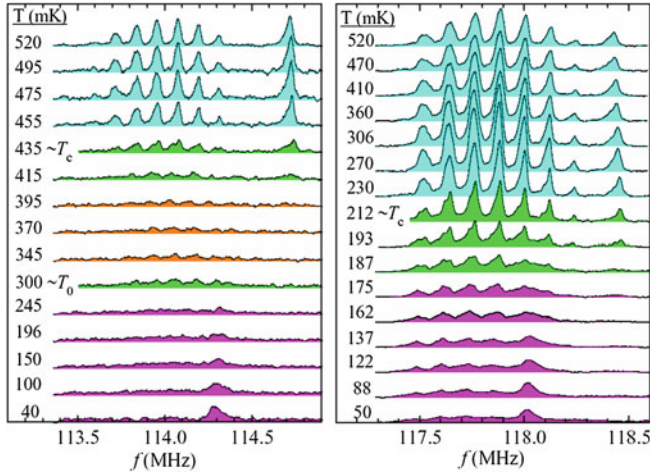


Fig. 1.14 NMR spectra of the Co and the In(1) site in CeCoIn₅ acquired in a field of 11.1 T (*left*) and 11.485 T (*right*). The *light blue* spectra are in the normal state, the *green* are within 20 mK of a phase transition, the *orange* are in the mixed (vortex) phase, and the *purple* are in the field induced antiferromagnetic phase. Reproduced from [22]

(and hence the resonance frequency) due to the first order nature of the phase transition as the temperature is lowered through T_c . Deep within the Q phase, the In(1) and Co resonances are somewhat broadened and shifted, but remain relatively unaffected. For the In(2b) site the spectrum broadens by several MHz and develops a two-peaked pattern consistent with the presence of long range antiferromagnetic order. Several subsequent NMR and neutron scattering experiments confirmed the presence of this static antiferromagnetism [26–29].

The lack of splitting in the spectra of the In(1) and Co sites coupled with the broad double-peak structure of the In(2b) spectra place strong constraints on the possible magnetic structure. The spectrum is split into two peaks because the hyperfine field at the In(2b) site is either parallel or perpendicular to the applied field. However the relationship between the direction of the ordered Ce moments and that of the hyperfine field is non-trivial. Young et al. proposed a minimal model where the magnetic structure consists of ordered local Ce spins with moments \mathbf{S}_0 along the applied magnetic field direction (along [100]), with an ordering wavevector of the form $\mathbf{Q} = \pi(\frac{1+\delta}{a}, \frac{1}{a}, \frac{1}{c})$. The structure of the NMR spectra revealed the incommensurate nature, but the value of the modulation δ remained undetermined since the hyperfine field at the In(2) site depends on the product of the size of the ordered moment and the incommensuration. A more complete analysis of the static hyperfine fields that develop at each of these sites for different magnetic structures and orientations of the ordered Ce moments suggested that for $\mathbf{H} \parallel [100]$ the spins are oriented as $\mathbf{S}_0 \parallel [001]$ and the incommensurate wavevector is $\mathbf{Q}_i \perp \mathbf{S}_0$, as summarized in Fig. 1.16 [30]. Recent detailed studies of the evolution of the In(2b) spectrum as a function of temperature and field have revealed a continuous growth of the antiferromagnetic order parameter in this phase (see Fig. 1.17). The antiferromagnetic order parameter vanishes above H_{c2} , indicating that the physical origin of the Q phase is tied closely to the presence of the superconductivity.

Neutron diffraction experiments confirmed the presence of static long range incommensurate antiferromagnetism in the Q phase, both for the field along [100] and along [110], as well

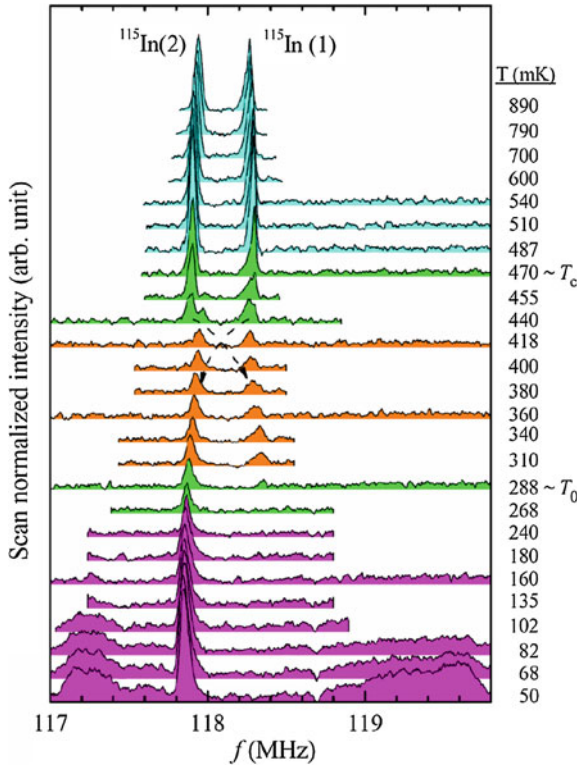


Fig. 1.15 Spectra of the In(1) and In(2b) in CeCoIn₅ acquired at 11.1 T. The In(1) transition shifts down in frequency below T_c , and the In(2b) shifts up due to the first order normal to superconducting phase transition. The In(2b) spectra develop two split peaks at low temperatures due to the antiferromagnetic ordering. Reproduced from [22]

as directly measured δ [31, 32]. A crucial observation was that δ is *independent of the applied field*, in contrast to the predictions for the FFLO phase. In an FFLO phase, the incommensurate wavevector of the superconducting order parameter is field dependent.

The discovery of static antiferromagnetism in this field induced phase has spurred considerable theoretical interest. A key question is whether the magnetic order is a consequence of an instability of the superconductivity that gives way to a more complex form of coexisting FFLO and antiferromagnetism, or whether the magnetism is tied to the proximity to a quantum critical point. A Ginzburg-Landau analysis of the coupled superconducting and antiferromagnetic order parameters, $\Delta(\mathbf{r})$ and $M(\mathbf{r})$, indicates that if the superconductivity develops modulations as prescribed by the FFLO scenario, then M can also develop such modulations [27]. Such a state may be described by pair density wave (PDW) condensate, which may also carry a small spin-triplet component [33–35]. An alternative description is that the antiferromagnetism develops as a spin density wave (SDW) between the Fermi pockets that emerge at the d-wave nodes of the superconducting order parameter [36]. In a magnetic field the Zeeman interaction shifts the quasiparticle spectrum such that the nodes develop into pockets. These pockets are nested, and since the normal state of this material already has strong

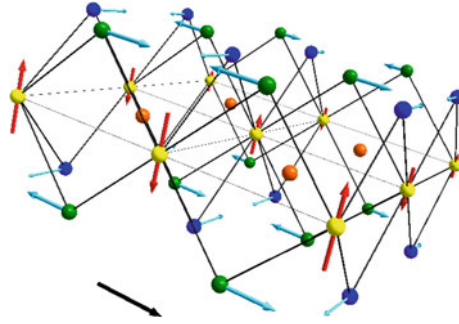
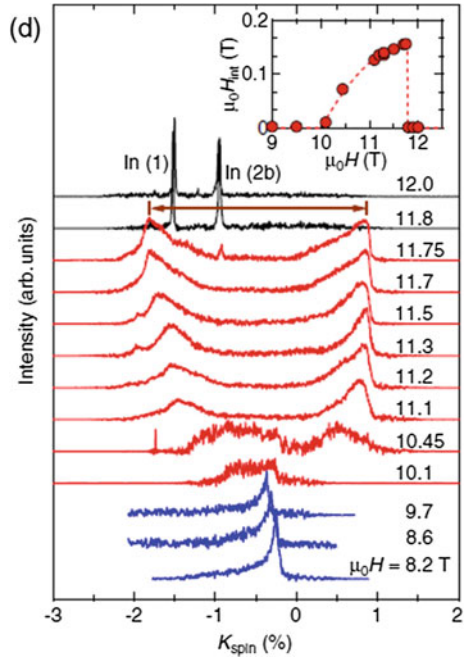


Fig. 1.16 Hyperfine fields and ordered moments in the field induced phase of CeCoIn_5 . The in-plane tetragonal structure is outlined in gray. The Ce atoms are yellow, and their moments are indicated by red arrows pointing along [100]. The In(1) atoms are orange, and the Co are not shown. The In(2a) are blue and the In(2b) are green. The hyperfine fields are indicated by blue arrows, and the direction of \mathbf{B}_0 is shown by the black arrow. Reproduced from [30]

Fig. 1.17 Spectra of the In(1) and In(2b) at several different fields at 50 mK. The inset shows the temperature dependence of the internal field at the In(2b) site. Reproduced from [29]



antiferromagnetic fluctuations at the wavevector $\mathbf{Q} = (\pi/a, \pi/a)$ the quasiparticles can form an SDW. In this picture the superconducting order parameter is not modulated. Furthermore this scenario is consistent with the observation that the ordering wavevector \mathbf{Q} is independent of the orientation of the field in the plane [32].

In summary, NMR has played a crucial role in the discovery and subsequent characterization of the field induced phase of CeCoIn_5 , illustrating a fascinating example of correlated

electron behavior in condensed matter. At present there remains no consensus as to the origin of the antiferromagnetism, which emerges in a region of parameter space where the Zeeman energy of the electrons, the superconducting condensate energy, and the Kondo exchange between the local moments and the conduction electrons are all on the same order of magnitude. Furthermore, recent detailed NMR studies of the In(1) and In(2a) sites suggest that the superconducting order parameter $\Delta(\mathbf{r})$ may also be spatially modulated [29]. It is unclear, however, that the length scale of such a modulation is tied with that of the antiferromagnetism, or if this behavior reflects a more complex FFLO state. In addition, recent NMR data has suggested an unusual behavior of the vortex lattice phase in fields $H_{c1} < H < H^*$, where $H^* \approx 10$ T low field boundary of the Q phase [28]. For moderate fields the NMR linewidth is significantly broader than that expected for a conventional Abrikosov vortex lattice, and it has been suggested that there is yet another phase present in this field range. It remains unclear whether these observations are consistent with a true thermodynamic phase or are a manifestation of slow spin fluctuations close to the phase boundary. Undoubtedly further NMR work will continue to reveal new information about this exotic new phase of strongly correlated electron matter.

References

1. C.P. Slichter, *Principles of Nuclear Magnetic Resonance*, 3rd edn. (Springer, New York, 1992)
2. E.L. Hahn, Phys. Rev. **80**, 580 (1950)
3. J. Haase, M.S. Conradi, Chem. Phys. Lett. **209**(3), 287 (1993)
4. A.M. Clogston, V. Jaccarino, Phys. Rev. **121**(5), 1357 (1961)
5. R.E. Walstedt, R.F. Bell, L.F. Schneemeyer, J.V. Waszczak, G.P. Espinosa, Phys. Rev. B **45**(14), 8074 (1992)
6. N.J. Curro, Rep. Prog. Phys. **72**(2), 026502 (24pp) (2009)
7. N.J. Curro, B.L. Young, J. Schmalian, D. Pines, Phys. Rev. B **70**(23), 235117 (2004)
8. N.J. Curro, B. Simovic, P.C. Hammel, P.G. Pagliuso, J.L. Sarrao, J.D. Thompson, G.B. Martins, Phys. Rev. B **64**(18), 180514 (2001)
9. Y.F. Yang, Z. Fisk, H.O. Lee, J.D. Thompson, D. Pines, Nature **454**, 611 (2008)
10. D. Pines, Phys. Rev. **95**(4), 1090 (1954)
11. A. Bianchi, R. Movshovich, C. Capan, P.G. Pagliuso, J.L. Sarrao, Phys. Rev. Lett. **91**(18), 187004 (2003)
12. T. Moriya, J. Phys. Soc. Jpn. **18**(4), 516 (1963)
13. S.E. Barrett, J.A. Martindale, D.J. Durand, C.H. Pennington, C.P. Slichter, T.A. Friedmann, J.P. Rice, D.M. Ginsberg, Phys. Rev. Lett. **66**(1), 108 (1991)
14. C. Petrovic, R. Movshovich, M. Jaime, P.G. Pagliuso, M.F. Hundley, J.L. Sarrao, Z. Fisk, J.D. Thompson, Europhys. Lett. **53**(3), 354 (2001)
15. K. Maki, T. Tsuneto, Prog. Theor. Phys. **31**, 945 (1964)
16. P. Fulde, R.A. Ferrell, Phys. Rev. **135**, A550 (1964)
17. A.I. Larkin, Y.N. Ovchinnikov, Sov. Phys. JETP **20**, 762 (1965)
18. A.B. Vorontsov, M.J. Graf, Phys. Rev. B **74**, 172504 (2006)
19. A. Bianchi, R. Movshovich, N. Oeschler, P. Gegenwart, F. Steglich, J.D. Thompson, P.G. Pagliuso, J.L. Sarrao, Phys. Rev. Lett. **89**(13), 137002 (2002)
20. H.A. Radovan, N.A. Fortune, T.P. Murphy, S.T. Hannahs, E.C. Palm, S.W. Tozer, D. Hall, Nature **425**, 51 (2003)
21. K. Kakuyanagi, M. Saitoh, K. Kumagai, S. Takashima, M. Nohara, H. Takagi, Y. Matsuda, Phys. Rev. Lett. **94**(4), 047602 (2005)
22. B.L. Young, R.R. Urbano, N.J. Curro, J.D. Thompson, J.L. Sarrao, A.B. Vorontsov, M.J. Graf, Phys. Rev. Lett. **98**, 036402 (2007)

23. V.F. Mitrović, G. Koutroulakis, M. Klanjšek, M. Horvatić, C. Berthier, G. Knebel, G. Lapertot, J. Flouquet, *Phys. Rev. Lett.* **101**(3), 039701 (2008)
24. V.F. Mitrovic, M. Horvatic, C. Berthier, G. Knebel, G. Lapertot, J. Flouquet, *Phys. Rev. Lett.* **97**(11), 117002 (2006)
25. A.B. Vorontsov, M.J. Graf, in *AIP Conference Proceedings* LT24 850, 729 (2006)
26. G. Koutroulakis, V.F. Mitrović, M. Horvatić, C. Berthier, G. Lapertot, J. Flouquet, *Phys. Rev. Lett.* **101**(4), 047004 (2008)
27. M. Kenzelmann, T. Strassle, C. Niedermayer, M. Sigrist, B. Padmanabhan, M. Zolliker, A.D. Bianchi, R. Movshovich, E.D. Bauer, J.L. Sarrao, J.D. Thompson, *Science* **321**(5896), 1652 (2008)
28. G. Koutroulakis, M.D. Stewart, V.F. Mitrović, M. Horvatić, C. Berthier, G. Lapertot, J. Flouquet, *Phys. Rev. Lett.* **104**, 087001 (2010)
29. K. Kumagai, H. Shishido, T. Shibauchi, Y. Matsuda, *Phys. Rev. Lett.* **106**, 137004 (2011)
30. N.J. Curro, B.L. Young, R.R. Urbano, M.J. Graf, *J. Low Temp. Phys.* **2010**, 635 (2009)
31. A.D. Bianchi, M. Kenzelmann, L. DeBeer-Schmitt, J.S. White, E.M. Forgan, J. Mesot, M. Zolliker, J. Kohlbrecher, R. Movshovich, E.D. Bauer, J.L. Sarrao, Z. Fisk, C. Petrovic, M.R. Eskildsen, *Science* **319**, 177 (2008)
32. M. Kenzelmann, S. Gerber, N. Egetenmeyer, J.L. Gavilano, T. Strässle, A.D. Bianchi, E. Ressouche, R. Movshovich, E.D. Bauer, J.L. Sarrao, J.D. Thompson, *Phys. Rev. Lett.* **104**, 127001 (2010)
33. D.F. Agterberg, M. Sigrist, H. Tsunetsugu, *Phys. Rev. Lett.* **102**(20), 207004 (2009)
34. A. Aperis, G. Varelogiannis, P.B. Littlewood, *Phys. Rev. Lett.* **104**, 216403 (2010)
35. Y. Yanase, M. Sigrist, *J. Phys. Soc. Jpn.* **78**(11), 114715 (2009)
36. Y. Kato, C.D. Batista, I. Vekhter, *Phys. Rev. Lett.* **107**, 096401 (2011)

Strongly Correlated Systems

Experimental Techniques

Avella, A.; Mancini, F. (Eds.)

2015, XXXIII, 302 p. 117 illus., 74 illus. in color.,

Hardcover

ISBN: 978-3-662-44132-9